

Photonic entanglement enhanced multidimensional spectroscopy for probing exciton correlations: theory and applications to photosynthetic aggregates

Arunangshu Debnath^{1,*} and Shaul Mukamel^{2,†}

¹*Center for Free-Electron Laser Science CFEL, Deutsches Elektronen-Synchrotron DESY, Notkestrasse 85, 22607 Hamburg, Germany*

²*Department of Chemistry and Department of Physics and Astronomy, University of California, Irvine, California 92697, USA*

(Dated: February 6, 2026)

Nonlinear spectroscopic techniques using entangled photon pairs provide an opportunity to exploit non-classical correlations encoded in two-photon wavefunctions to manipulate two-exciton wavefunctions. We propose an entangled photon pair-enhanced multidimensional spectroscopic technique which is sensitive to exciton-exciton interactions and correlations at the ultrafast timescale. Simulations for a dissipative photosynthetic aggregate reveal the superior ability of entangled photon pairs, compared to both transform-limited and frequency-chirped laser pulses, to manipulate excited-state absorption pathways. The corresponding spectral features in the two-dimensional spectrogram are interpreted in terms of one- and two-exciton resonances. The signal scales linearly with the incoming intensity of the photon sources. It is argued that classifying these resonances using entangled photon source at the perturbative limit allow for probing exciton correlations at the natural energy scale. These insights can be used to explore multi-exciton dynamics using multiphoton entanglement.

I. INTRODUCTION

In molecular aggregates, spectroscopic characterization of exciton-exciton interactions and correlations yields critical insights into underlying aggregation properties. However, the range of spectroscopic techniques available for exploring their temporal and spectral signatures, particularly in the presence of phonon-induced dissipation, remains limited. These challenges stem, in part, from a lack of techniques specifically tailored to extract correlation induced features hidden in the dynamics of spatially delocalized two-exciton states. Double-quantum coherence (DQC), a nonlinear spectroscopic scheme, was proposed as a viable approach for probing quasiparticle correlation and their dynamical signatures [1–4]. Among the suite of nonlinear spectroscopic techniques classified as four-wave mixing, photon echo and transient grating primarily investigate ultrafast exciton transport. Although the observed signals may contain contributions from two-exciton states, the associated resonances are often obscured by dominant one-exciton resonances. The double-quantum coherence technique investigates spectral features specifically associated with two-exciton states; the observed signal is sensitive to the differential nature of the two-exciton wavefunction compared to that of the constituent two one-exciton wavefunctions [5, 6]. In previous investigations, double-quantum coherence spectroscopy has aided the exploration of quasiparticle correlations in molecular aggregates [2, 7], quantum-confined nanostructures [6, 8], correlated lattice systems [9], atomic gases [10–12], coupled valence and core-hole excitations in molecules [13], vibrations [14], exciton and vibrational polaritons [15–18].

In this article, we deploy the DQC technique to characterize the ultrafast dynamics of molecular exciton aggregates, specifically identifying the resonances that originate from exciton-exciton interactions and correlations. DQC probes the ultrafast dynamics of the two-exciton wavefunctions via interfering contributions of excited-state absorption (ESA) pathways. Primary signatures of exciton correlations are typically hidden in the two-exciton states, making the technique an ideal candidate to monitor and classify correlation-induced resonances.

For the simulation of the signal, we focus on the light-harvesting complex, LHCII, which acts as the primary photon energy harvester in photosynthetic aggregates. LHCII hosts a large number of one- and two-exciton states delocalized over sites, each of which undergo ultrafast dephasing due to interaction with phonons. As a result, the spectroscopic identification of correlation-induced resonances become particularly challenging. In principle, pulse-shaping techniques are expected to address two-exciton resonances and selectively amplify desired signal components. However, given the relatively high density of optical transitions within a narrow spectral range, classical laser sources face significant challenges. These challenges stem from the unavoidable time-frequency bandwidth constraints. The situation becomes even more critical when identical exciton transitions possess comparable dephasing rates. The entangled photon sources promise to partially alleviate some of these obstacles [15, 16, 19–27], even though identifying a

* arunangshu.debnath@desy.de

† smukamel@uci.edu

suitable parameter regime where entangled photon pairs outperform their classical counterparts remains a challenging endeavor [28, 29].

We demonstrate that the entangled-photon-pair enhanced DQC technique, which utilizes the correlation properties

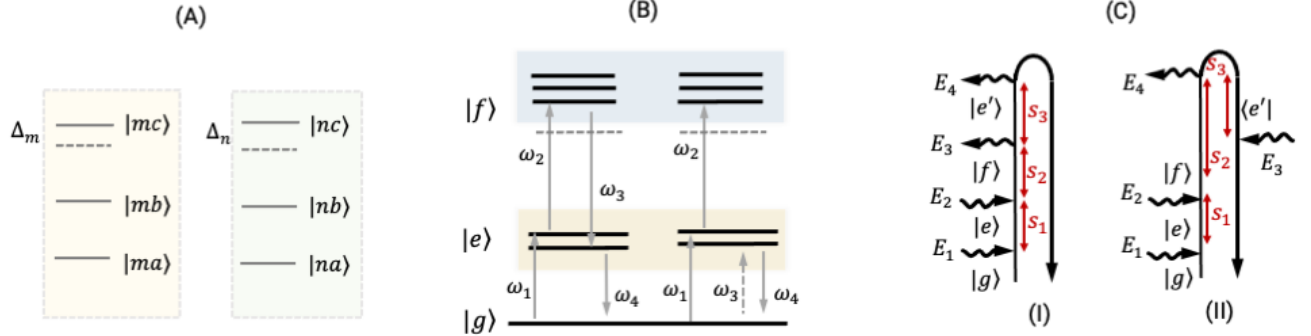


FIG. 1: (A) Simplified schematic description of two interacting exciton levels (denoted $|j\rangle$, where $j \in \{a, b, c\}$) at sites m, n highlighting exciton nonlinearities (denoted Δ_m, Δ_n). The simulation contains 14 such sites. In the delocalized basis, the two-exciton states are affected by both overtone and combination nonlinearities. (B) The exciton pathways that contribute to the signal are presented using Albrecht notation. The process, involving ω_1 and ω_2 , is common to both pathways. The process, involving ω_3 and ω_4 , is discriminative depending on the differential nature of the two pathways. (C) The corresponding Keldysh-Schwinger diagram is presented.

of two-photon wavefunctions, may be suitable for manipulating two-exciton amplitudes. It is shown that a superior resolution of two-dimensional spectral features can be obtained compared to both transform-limited and linearly chirped pulses. Further, the spectral features are shown to be dependent on the variation of the exciton nonlinearity parameter, thus identifying their origin in exciton correlations.

In what follows, we introduce the exciton-phonon Hamiltonian of the monomeric LHCII, define the one- and two-exciton states, and derive the relevant Green's functions in section II A. Subsequently, in section III B, which is divided into three subsections, we present the analytical signal and corresponding numerical simulations. Simulations utilize entangled photon sources, classical laser pulses, and a variation of the exciton nonlinearity parameters. The article concludes in section IV with a summary and an outlook.

II. THEORY

A. Hamiltonian

We construct a description of LHCII monomer, using the Frenkel exciton model within the Heitler-London approximation. For this purpose, we take the lowest-lying adiabatic electronic states of each of the $N_s = 14$ chromophoric sites containing chlorophyll molecules. The combined exciton-phonon Hamiltonian, in the site basis, is given by

$$H = \sum_{mn} (E_m \delta_{mn} + J_{mn}) B_m^\dagger B_n \quad (1a)$$

$$+ \sum_{mn} U_m^{(1)} B_m^\dagger B_m^\dagger B_m B_m + U_{mn}^{(2)} B_m^\dagger B_n^\dagger B_n B_m \quad (1b)$$

$$+ \sum_j \omega_j (b_j^\dagger b_j + \frac{1}{2}) + \sum_{m,j} g_{m,j} (b_j^\dagger + b_j) B_m^\dagger B_m \quad (1c)$$

where $B_m^\dagger (B_m)$ represent the exciton creation (annihilation) operators, which follow the commutation relation $[B_n, B_m^\dagger] = \delta_{mn}(1 - \eta(B_m^\dagger B_m)^2)$ (where $\eta = 3/2$). Parameters E_m , J_{mn} , $U_m^{(1)}$, and $U_{mn}^{(2)}$ represents one-exciton energy, and inter-site hopping, overtone, and combination exciton non-linearity parameters, respectively. $H_{mn}^{(1)} = \sum_{mn} (E_m \delta_{mn} + J_{mn})$ denotes the one-exciton Hamiltonian matrix elements, while $H_{mnkl}^{(2)} = H_{mn}^{(1)} \delta_{kl} + \delta_{mn} H_{kl}^{(1)} + U_m^{(1)} + U_{mn}^{(2)}$ denote their two-exciton counterparts. While, all parameters J_{mn} , $U_m^{(1)}$ and $U_{mn}^{(2)}$ affect the overtone and combination two-exciton states, the latter two are responsible for the shift in two-exciton energies. It can be expressed as $E_m^{(2)} = 2E_m^{(2)} + \Delta_m$ (where Δ_m is negative is the two-exciton energy is stabilized). In the dipole approximation

for the charge densities, J_{mn} are determined by transition dipole moments and $U_m^{(1)}$, $U_{mn}^{(2)}$ by the difference of the permanent dipole moments between the excited state and the ground state. Previous theoretical investigations involving two-exciton states which uses coupled two-level models have omitted the role of the overtone states. While arguments based on the laser bandwidth, may allow one to approximate the two-exciton manifold, it would amount to neglecting the role of permanent dipole moments altogether. For chlorophyll molecules, the key pigment in LHCII, the excited state permanent dipole moment is often comparable to their transition dipole moment.

The Hamiltonian yields $N_g = 1$ ground state, $N_e = 14$ one-exciton states, and $N_f = 105$ two-exciton states; the latter is composed of 14 overtone and 91 combination states. The exciton part of the Hamiltonian, given in the first two lines of Eq. (1), can be diagonalized to yield exciton-number-conserving manifolds, denoted as $|g\rangle$, $|e\rangle$, and $|f\rangle$. These states are expressed as $|e_j\rangle = \sum_m T_{j,m}^{(1)} B_m^\dagger |0\rangle$ and $|f_k\rangle = \sum_{m,n} T_{k,mn}^{(2)} B_m^\dagger B_n^\dagger |0\rangle$. The transformation matrix elements, $T_{j,m}^{(1)}$ and $T_{k,mn}^{(2)}$, determine the degree of exciton delocalization for a given exciton state. The exciton states are coupled to collective vibrational modes—the normal modes of intermolecular vibrations—hereafter referred to as phonons. The bare phonon and exciton-phonon coupling Hamiltonians are defined in the third line of Eq. (1). Here, the phonon-mode creation (annihilation) operators b_j^\dagger (b_j) follow free-boson commutation relations, defined as $[b_j, b_i^\dagger] = \delta_{ij}$, while $g_{m,j}$ represents the site-specific coupling strengths. For LHCII, the phonon spectral density function comprises $N_{b_2} = 48$ high-frequency Brownian oscillator modes and $N_{b_1} = 1$ low-frequency, overdamped Brownian oscillator mode, expressed as:

$$J_{\text{ph}}(\omega) = 2\lambda_0 \frac{\omega\gamma_0}{\omega^2 + \gamma_0^2} + \sum_{j=1}^{N_{b_2}} \frac{2\lambda_j\omega_j^2\omega\gamma_j}{(\omega_j^2 - \omega^2)^2 + \omega^2\gamma_j^2} \quad (2)$$

The associated parameter values are adopted from [15, 16, 30, 31]. All simulations were performed at a temperature of $T = 273$ K.

The photon-exciton interaction Hamiltonian is given by

$$H_{\text{int}}(t) = EV^\dagger + E^\dagger V = \sum_{j,pq \in \{ge,ef\}} \sqrt{\frac{2\pi\omega_j}{V}} \left(a_j \exp(-i\omega_j t) \exp(i\omega_{pq} t) d_{pq} |p\rangle\langle q| + \text{h.c.} \right) \quad (3)$$

The photonic sources probe the excitonic dynamics by inducing transitions between the exciton manifolds; these are captured by the inter-manifold transition operator $V^\dagger = d_{pq} |p\rangle\langle q|$, where ω_{pq} denotes the exciton energy gap. If the photonic sources can be manipulated with a high degree of control, the inter-manifold exciton transitions and corresponding resonances can be probed in a systematic manner.

The Green's functions are defined as $\mathcal{G}_{pq}(\omega) = i(\omega - z_{pq})^{-1}$, where the exciton resonances associated with inter-manifold transitions are given by $z_{pq} = \omega_{ab} + i\Gamma_{pq}$. The energy gaps, ω_{ab} and inter-manifold dephasing parameters, Γ_{pq} , jointly determine the locations of these resonances. The dephasing parameters are estimated using the line-broadening function, $\Gamma_{pq} = (\gamma_p + \gamma_{q'})/2$, where

$$\gamma_p(t) = \sum_{p'} C_{\text{ph}}(\Omega_{pp'}) \sum_m T_{mp} T_{mp} T_{mp'} T_{mp'} \quad (4)$$

Here, the thermally weighted phonon spectral density, evaluated at the energy gap $\Omega_{pp'}$, is given by

$$C_{\text{ph}}(\Omega) = \int_0^\infty dt \exp(i\Omega t) \times \int \frac{d\omega}{2\pi} J(\omega) \left[\coth(\beta\omega/2) \cos\omega t \mp i \sin\omega t \right] \quad (5)$$

This dephasing properties are determined by the resonant phonon modes.

III. RESULTS

A. Theory

The DQC signal is related to a specific component of the excitonic nonlinear polarization, $k_s = +k_1 + k_2 - k_3$ generated as a result of four exciton-photon interactions (see Fig. 1). Following the derivation outlined in the appendix, the final expression is obtained as

$$S(\Omega_3, \Omega_2, \Omega_1) = s_0 \sum_{f, e', e, g} w^{(1)} \frac{\langle E_4^\dagger(w_{e'f}) E_3^\dagger(w_{e'g}) E_2(w_{fe}) E_1(w_{eg}) \rangle}{\tilde{F}_\Omega^{(1)}(\Omega_3, \Omega_2, \Omega_1; z_{e'g}, z_{fg}, z_{eg})} + w^{(2)} \frac{\langle E_4^\dagger(w_{ge'}) E_3^\dagger(w_{e'f}) E_2(w_{fe}) E_1(w_{eg}) \rangle}{\tilde{F}_\Omega^{(2)}(\Omega_3, \Omega_2, \Omega_1; z_{fe'}, z_{fg}, z_{eg})}. \quad (6)$$

where the proportionality constant s_0 incorporates all the coefficients in the expression and serves as a scaling parameter in the numerical simulation. In the expression, the dipolar spectral weights associated with the two pathways are given by: $w^{(1)} = d_{e'f} d_{e'g} d_{fe} d_{eg}$ and $w^{(2)} = d_{ge'} d_{e'f} d_{fe} d_{eg}$. We also introduced two multidimensional functions of the following form

$$\begin{aligned} \tilde{F}_\Omega(\Omega_3, \Omega_2, \Omega_1; z_c, z_b, z_a) = \\ (\Omega_3 - z_c)(\Omega_2 - z_b)(\Omega_1 - z_a) \end{aligned} \quad (7)$$

The variables, Ω_j , can be scanned to identify and track excitonic resonances. In a typical two-dimensional spectrum (plotted with Ω_2 and Ω_3 as parametric axes for a fixed Ω_1), the off-diagonal spectral features primarily correspond to the spectral signatures that having its origin in exciton interactions and correlations. The four-point photon correlation correlation functions in the numerator allow the modulation of respective spectral weights.

Spontaneous parametric down-conversion (SPDC) provides a control knob for external manipulation of the two-photon wavefunction and the correlation function [32, 33]. In the weak down-conversion regime, the photon correlation function is given by: $\langle E^\dagger(\omega_4) E^\dagger(\omega_4) E(\omega_2) E(\omega_1) \rangle = f^*(\omega_4, \omega_3) f(\omega_2, \omega_1)$, where we define the joint spectral amplitude (JSA) of the two-photon field

$$\begin{aligned} f(\omega_a, \omega_b) = \alpha A_p(\omega_a, \omega_b) \\ \times \left\{ \text{sinc}[\phi(\omega_a, \omega_b)] \times \exp i\phi(\omega_a, \omega_b) + a \leftrightarrow b \right\} \end{aligned} \quad (8)$$

$A_p(\omega_a, \omega_b)$ is the transform-limited field profile of the SPDC pump taken as $A_p(\omega_a, \omega_b) = E_0 \sqrt{\pi/\Gamma_{p,0}} \exp [-(\omega - \omega_a - \omega_b)^2/4\Gamma_{p,0}]$, where $\Gamma_{p,0}$ is the temporal width. The parameter α governs the down-conversion efficiency. The phase function $\phi(\omega_j, \omega_k) = (\omega_j - \omega_p/2)T_1 + (\omega_k - \omega_p/2)T_2$ is governed by the entanglement time parameter $T_{\text{ent}} = |T_2 - T_1|$. The latter is crucial for spectroscopic applications and is determined by the SPDC crystal length and the relative group velocities of the photons within the crystal. The square modulus of the JSA, depicted in Fig. 6, shows that for strongly anti-correlated pairs, there is parametric freedom to select two distant frequency values. During ultrafast measurements, this flexibility imposes less stringent conditions on the entangled photon pair frequencies. The associated singular values, also presented in Fig. 6, can be used to estimate the effective correlation between spectral modes [25, 28, 34]. The four-point field correlation function for classical laser pulses factorizes into the product of individual amplitude functions, given by: $\langle E^\dagger(\omega_4) E^\dagger(\omega_3) E(\omega_2) E(\omega_1) \rangle = A_{p_4}^*(\omega_4) A_{p_3}^*(\omega_3) A_{p_2}(\omega_2) A_{p_1}(\omega_1)$. The signal, therefore, scales quadratically with the intensity of the incident field. The profile for the linearly chirped pulse is defined as:

$$A_{p_i}(\omega) = E_0 \sqrt{\pi/\Gamma_{0,i}} \exp [-(\omega - \omega_{0,i})^2/4\Gamma_i] \quad (9)$$

Here, $1/\Gamma = 1/\Gamma_0 - 2i\phi_0^{(2)}$, where $\phi_0^{(2)}$ denotes the linear chirp rate and $\Gamma_0 = 2 \ln(2)/\tau_0$ is determined by the temporal pulse width, τ_0 [35–37]. Setting the chirp parameter to zero ($\phi_0^{(2)} = 0$) yields a transform-limited laser pulse.

The generation of the DQC signal can be conceptualized as a combination of two processes: the initial formation of a state-specific two-exciton coherence, followed by the subsequent projection of these coherent oscillations onto one of two possible one-exciton coherence components. Each of the two pathways depicted in Fig. 1 represents this phenomenology, wherein the two-exciton coherence is generated during the interval $s_1 + s_2$, and the distinct one-exciton coherence are selected during the final interval s_3 . We can manipulate the corresponding two-exciton resonances, z_{fg} , by modulating the sum frequency $\omega_p = \omega_1 + \omega_2$ during the initial pair of exciton-photon interactions. We can also manipulate the resonances at either $z_{e'g}$ or $z_{fe'}$ during the subsequent pair of exciton-photon interactions by modulating ω_3 and ω_4 . The final signal is the resultant of two interfering pathways, the magnitude of which is largely determined by these last two interactions. If the contributions from exciton nonlinearities are not significant, the resonances $z_{e'g}$ and $z_{fe'}$ yield nearly identical contributions. Under these conditions, $z_{fe'} \approx \omega_{e'g} + \Delta + i\Gamma_{fe'} \approx \omega_{e'g} + i\Gamma_{fe'}$, where the energetic deviation Δ is negligible. Consequently, the two pathways interfere destructively, and the spectral weights diminish toward zero.

B. Simulations

Strategies for observing desired spectroscopic features can be devised by jointly considering the exciton gaps $\omega_{pp'}$ and the dephasing parameters $\Gamma_{pp'}$. They jointly contribute to the inter-manifold exciton resonances: $z_{pp'}$, defined earlier.

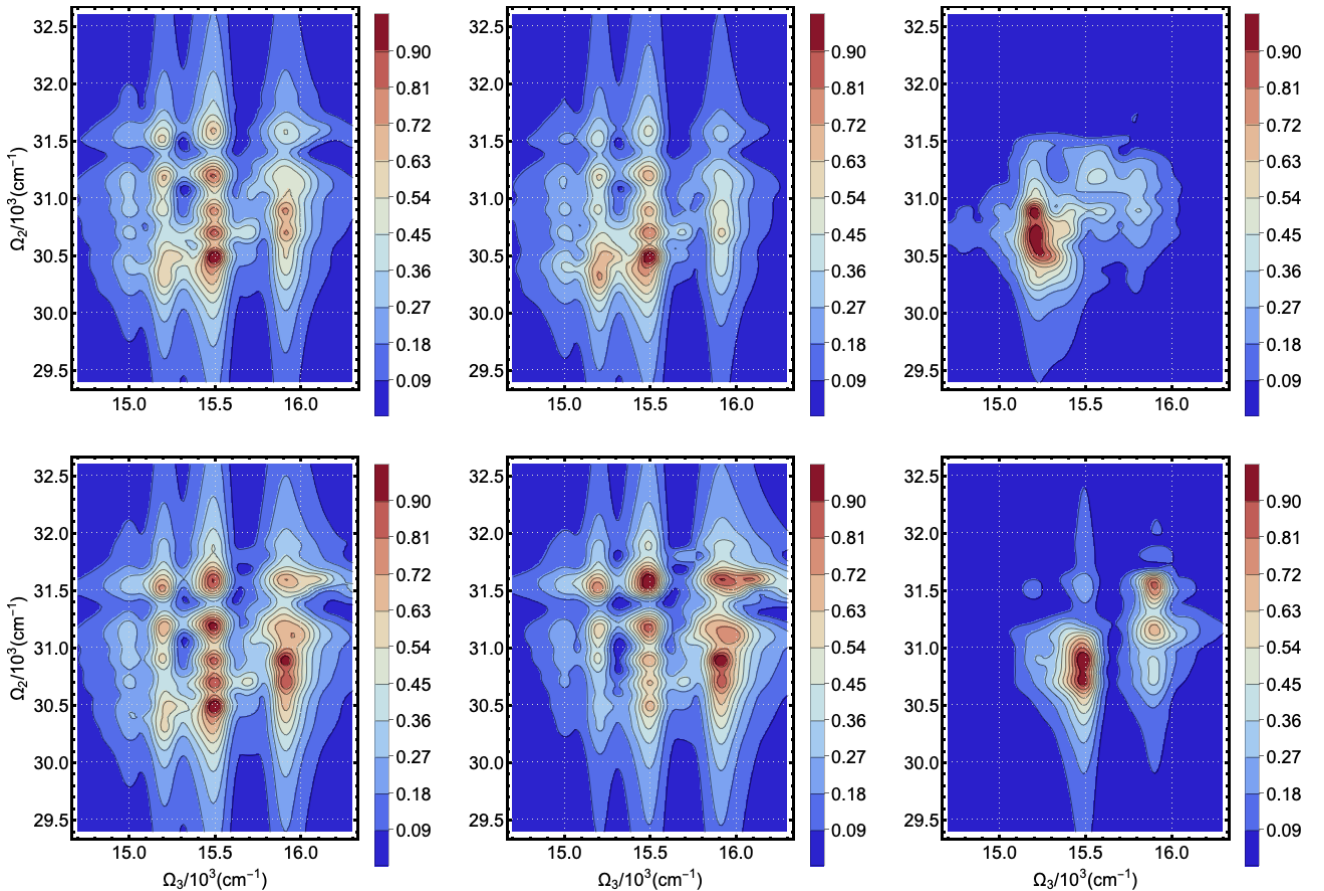


FIG. 2: Simulated DQC spectra using entangled photon pairs. The sum frequencies of the photon pairs are tuned to the two-exciton states f_{39} (top panel) and f_{81} (bottom panel). The left column provides a reference simulation with an entanglement time $T_{\text{ent}} = 10$ fs and an SPDC pump temporal width $\tau_0 = 50$ fs. The middle column shows the effects of varying the SPDC pump temporal width, while the right column shows the effects of varying the entanglement time relative to the references. For a detailed discussion, see Section III B 1.

In an ideal scenario, scanning the Ω_2 axis would maximally display $N(N - 1)/2 + N = 105$ number of z_{fg} resonances, while scanning the Ω_3 axis would display a mixture of z_{fe} and z_{eg} resonances, amounting to $(N(N - 1)/2 + N)N = 105 \times 14$, and $N = 14$, resonances respectively. In general, a high density of optical transitions makes it difficult to control individual spectral features independently. Additionally, the presence of dephasing causes several resonances to overlap. The external photonic sources may also mask several resonances depending on its spectral bandwidth properties. While intuition suggests that a narrowband source is a reasonable choice for generating state-specific two-exciton coherence, it may face challenges by the ultrafast dephasing of the mediating one-exciton states. Similarly, the selective projection to one-exciton coherence using a narrowband source can be less discriminating if the state transitions involved have similar spectral weights. These problems can be partially mitigated by exploiting the properties of the entangled photon pairs.

In the following, we present the numerical simulation across three subsections. First, we deploy entangled photon pairs to explore correlations encoded in a two-exciton state by exciting them via a chosen pair of one-exciton states. Two such cases are explored, for each of which we choose a different pair of mediating one-exciton states. Second, we use a transform-limited and a frequency-chirped pulse in an attempt to recover the spectral features observed in the first case. One principal aim of this study is to recover maximal number of exciton resonances observed in the previous case by using both broadband and narrowband classical photonic sources. Third, we repeat the simulation for two different exciton nonlinearity parameters (the parameter quantifying exciton correlation within the Frenkel exciton model) and using degenerate laser pulses. This study is aimed at exploring the alteration of spectral features previously observed.

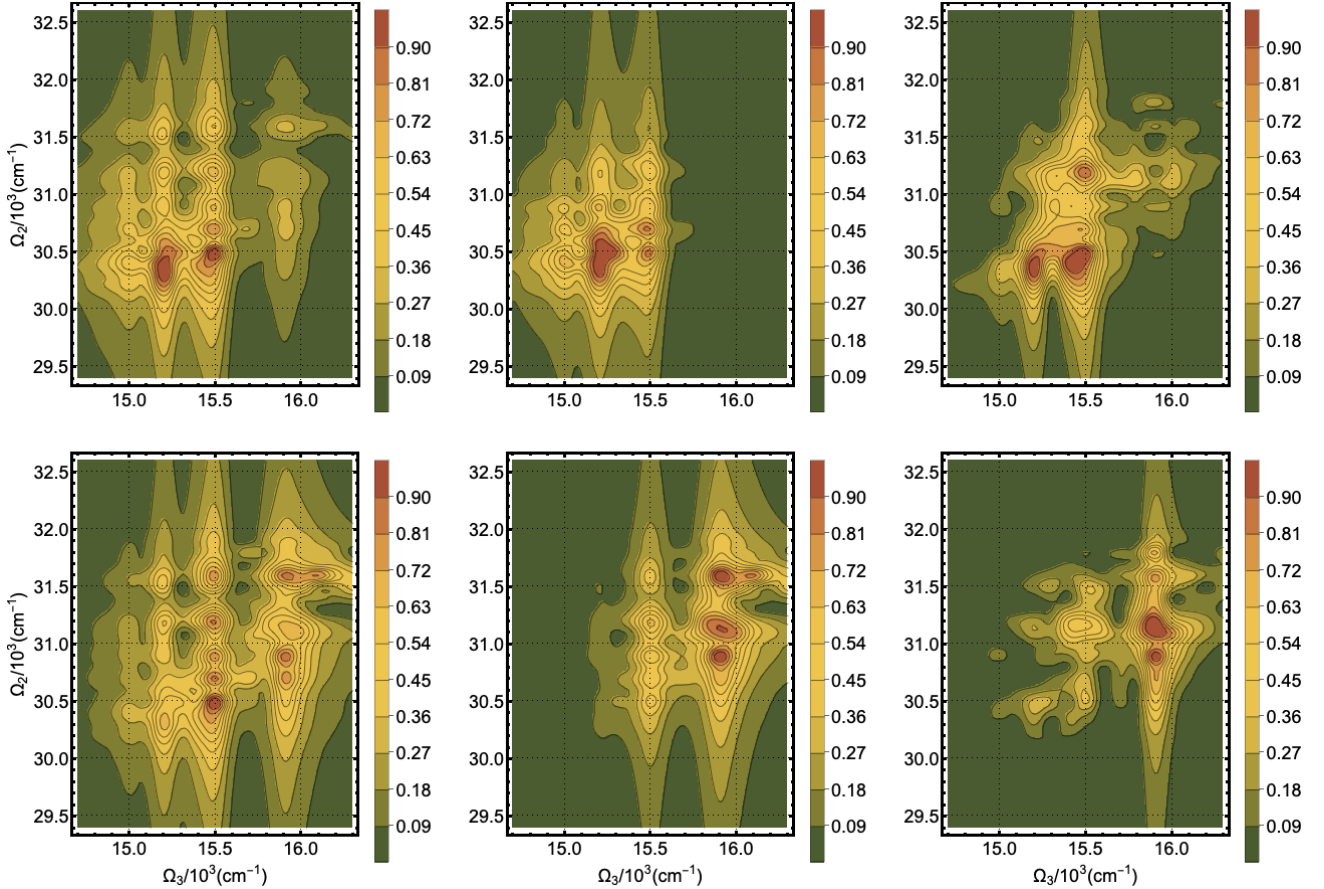


FIG. 3: Simulated DQC spectra using classical laser pulses. The central frequencies match the parameters employed for the entangled photon pairs in Fig. 2. The left column presents reference simulations with a temporal width of $\tau_{j,0} = 10$ fs. The middle column shows the effect of an increased temporal width ($\tau_{j,0} = 20$ fs), which decreases the spectral bandwidth and suppresses several resonances. The right column displays spectra obtained using linearly chirped pulses; notably, the negatively chirped pulse was unable to recover the suppressed resonances. For a detailed discussion, see Section III B 2.

1. DQC spectra with entangled photon pairs

We present the simulated two-dimensional spectra obtained using entangled photon pairs in Fig. 2. Two distinct two-exciton states, f_{39} and f_{81} , are targeted by tuning the sum frequency ω_p to the respective state energies (top and bottom panels, respectively). Furthermore, the frequencies of the entangled photon pairs are chosen such that $\omega_1 = \omega_3$ and $\omega_2 = \omega_4$. This implies that the first pair of photons is identical to the second in the simulation. Additionally, we apply the following energy matching conditions: $\omega_1 \approx E_{e_{05}}$ and $\omega_2 \approx E_{e_{09}}$ for the top panel (with $\omega_p \approx E_{f_{39}}$), and $\omega_1 \approx E_{e_{07}}$ and $\omega_2 \approx E_{e_{13}}$ for the bottom panel (with $\omega_p \approx E_{f_{81}}$). The results presented in the left column (for both the upper and lower) serve as reference ($\tau_p = 50.0$ fs, $T_{\text{ent}} = 10$ fs). We intend to monitor the spectral variation with respect to the variation of temporal width of the SPDC pump ($\tau_p = 100.0$ fs for the top, and $\tau_p = 20.0$ fs for the bottom panel) and the entanglement time ($T_{\text{ent}} = 60$ fs), presented in the middle and right column, respectively. For each of these cases, all other parameters are kept the same as the reference.

The top-left panel shows dominant resonances partitioned into five sectors along the $\tilde{\Omega}_3$ axis and four sectors along the $\tilde{\Omega}_2$ axis (where $\tilde{\Omega} = \Omega/10^3$ in cm^{-1}). These features can be identified along the $\tilde{\Omega}_2$ axis at 31.5 ($\approx z_{f_{51}g}$), 30.9 ($\approx z_{f_{49}g}$), 30.4–30.5 ($\approx z_{f_{25}g} - z_{f_{27}g}$), and 30.2 ($\approx z_{f_{19}g}$). Identifying the resonances along the $\tilde{\Omega}_3$ axis is more difficult due to interfering contributions; however, we approximately identify the peaks with the following inter-manifold resonances: 15.0 ($\approx z_{f_{38}e_9} - z_{f_{38}e_{10}}$), 15.3 ($\approx z_{f_{38}e_8}, z_{f_{39}e_9}$), 15.5 ($\approx z_{f_{38}e_3}, z_{f_{39}e_3}, z_{f_{40}e_3}$), and 15.9–16.0 ($\approx z_{f_{41}e_4}$). In the top-middle panel, an increase in the temporal width produced noticeable changes by drastically reducing the spectral weights of several off-diagonal peaks. This reduction is attributed to destructive interference among the many pathways allowed by the larger bandwidth of the SPDC pump. In the top-right panel, increasing the entanglement

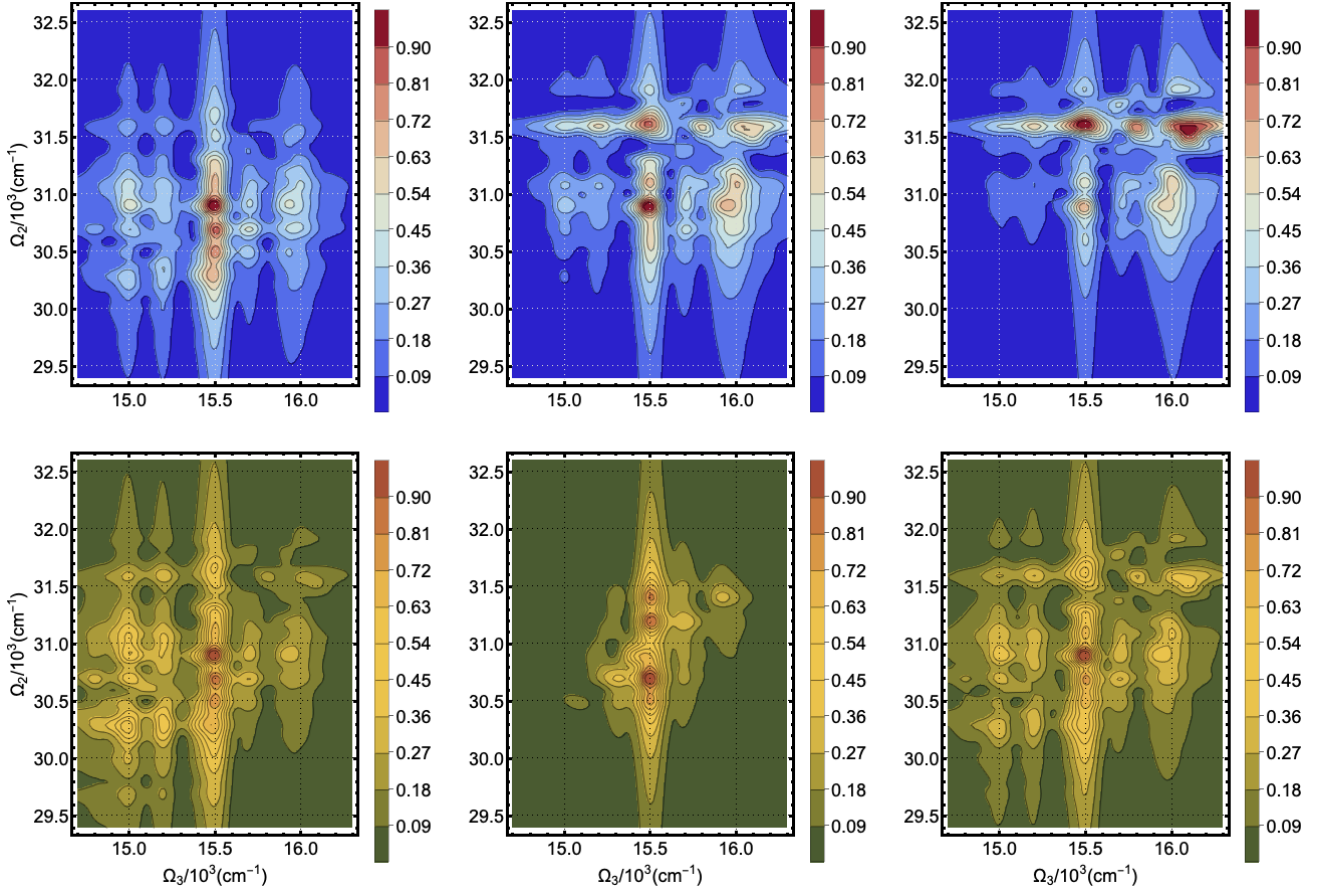


FIG. 4: Simulated DQC spectra using a variation of excitonic nonlinearity parameters which influences both the two-exciton wavefunction and the transition dipole moments. The lower (upper) panel presents the case for classical laser sources (entangled photon pairs). In the upper-left and upper-middle panel, using only higher overtone excitonic nonlinearities and two different two-exciton states are targeted using the same photonic parameter as in the reference simulation in Fig. 2. The upper-right uses degenerate entangled photon parameters to track the down-shifted resonances. The lower-left and lower-middle panel uses higher and lower overtone excitonic nonlinearities (compared to the results in Fig. 3) respectively. The lower-right employs degenerate pulse parameters to explore the down-shifted resonances. For detailed discussions, see Section III B 3.

time alters the intervals between successive exciton-photon interactions, which leads to the removal of off-diagonal spectral peaks. Consequently, only the resonance at $(\tilde{\Omega}_2, \tilde{\Omega}_3) \approx (30.9, 15.3)$ survives in the top-right panel, while $(\tilde{\Omega}_2, \tilde{\Omega}_3) \approx (31.3, 16.0)$ survives in the bottom-right panel.

The bottom-left panel exhibits resonances similar to those in the top-left panel, except for the off-diagonal resonances at $(\tilde{\Omega}_2, \tilde{\Omega}_3) \approx (31.5, 15.5)$ and within the range $(\tilde{\Omega}_2, \tilde{\Omega}_3) \approx (31.6-31.9, 16.0)$ which are enhanced. An interesting case emerges when increasing the temporal width of the SPDC pump: several off-diagonal peaks survive at $(\tilde{\Omega}_2, \tilde{\Omega}_3) \approx (31.5, 15.3)$, $(31.5, 15.5)$, $(30.7, 15.5)$, and $(30.7, 16.0)$. The bottom-right panel demonstrates a marked loss of resonances, with the exception of the surviving off-diagonal peak at $(\tilde{\Omega}_2, \tilde{\Omega}_3) \approx (31.3, 16.0)$. Overall, we note that the spectra in both panels retain their qualitative features along the $\tilde{\Omega}_3$ axis, even though they exhibit different prominent peaks along the $\tilde{\Omega}_2$ axis. In contrast to the top panel, the bottom panel exhibits reduced sensitivity to changes in the temporal width of the SPDC pump. This observation highlights that exciton correlation contributions manifest differently in these two cases.

2. DQC spectra with transformed limited and chirped laser pulses

In Fig. 3, we present the two-dimensional spectra simulated using two sets of laser pulses: transform-limited and chirped laser pulses, both characterized by a Gaussian profile. The central frequencies correspond to those utilized

for the entangled photon pairs, meaning that the targeted and mediating states remain consistent with those in Fig. 2. For the reference simulations, presented in the left column of both panels, we employ a transform-limited pulse with a temporal width of $\tau_{j,0} = 10$ fs. We intend to explore the spectral features resulting from the variation of the temporal width ($\tau_0 = 20$ fs) and the application of an additional spectral phase (a linear chirp parameter of -750 fs 2), presented in the middle and right columns, respectively. All other parameters remain identical to those of the reference simulation.

In the left column, we observe that compared to the previous simulations in Fig. 2, the number of resolved resonances is reduced, with this reduction being more prominent along the Ω_3 axis. Several spectral peaks exhibit significant broadening, and many carry diminished spectral weights. These features persist across all the plots. We also note that the upper-left panel exhibits a loss of a higher number of off-diagonal resonances compared to the lower one. In particular, the spectra in the upper-left, exhibit dominant resonances at $(\tilde{\Omega}_2; \tilde{\Omega}_3) \rightarrow (30.5; 15.5), (30.7; 15.5)$ which can be attributed as off-diagonal peaks. The longer temporal width of the pulses i.e., relatively narrowband case, in the upper-middle reveals that compared to the left ones, the majority of the peaks are absent at higher (at upper-middle) and lower (at lower-middle) values of $\tilde{\Omega}_3$. In the lower-middle, two peaks at $(\tilde{\Omega}_2; \tilde{\Omega}_3) \rightarrow (30.7; 16.0), (30.2; 16.0)$ gained spectral weights. In negatively chirped pulses, the instantaneous frequency decreases over time. In other words, the high-frequency components arrive earlier within the pulse profile. Such pulses were used to influence the discriminative step where stimulated emission to one-exciton states occurs. The inability of the parameters to explore more resonances is clearly reflected in the spectra, where we observe a few set of peaks i.e., $(\tilde{\Omega}_2; \tilde{\Omega}_3) \rightarrow (30.4; 15.5)$ (in the upper-right) and $(\tilde{\Omega}_2; \tilde{\Omega}_3) \rightarrow (31.2; 16.0)$ (in the lower-right) gaining significant spectral weights while others vanish. In drawing such a conclusion, we recall that the laser frequencies address the same mediating one-exciton states, making this specific combination of parameters, namely the chirp parameters and central frequencies, jointly unfavorable. It also highlights the dominant role played by two-exciton coherence generation as compared to the subsequent projection step.

3. DQC spectra for a variation of the exciton nonlinearity parameters and degenerate frequencies

As described by the second term of Eq. 6, the spectral peaks and their respective weights are dictated by interfering pathways. These pathways contain two inter-manifold resonances that correspond to the energy gaps $\omega_{fe'}$ and $\omega_{e'g}$; the differences between these gaps determine the signal. In the Frenkel exciton description, the observed differences are largely due to the exciton nonlinearity parameters $U_m^{(1)}$ and $U_m^{(2)}$. The exciton nonlinearities, while directly affecting the two-exciton eigenenergies, also changes the transformation matrices and, consequently, the resulting transition dipole moments. Figure 4 illustrates the influence of the variation of exciton nonlinearity parameter $U_m^{(1)}$ on the spectral features (left and middle columns). We also investigate the effect of degenerate frequencies of entangled photons (top-right) and classical lasers (bottom-right) to explore spectral changes caused by different $U_m^{(1)}$ values. Note that $U_m^{(1)}$ values were negative in previous sections, signifying the energetic stabilization of overtone two-exciton energies; the distribution of these values is shown in Fig. 5.

The upper-left and upper-middle panels repeat the reference simulation from Fig. 2, setting the nonlinearity parameter $U_m^{(1)}$ to a higher (increasing them to the values depicted in Fig. 5) and lower values (lowering them to one-order of magnitude), respectively. Changing the magnitude of the $U_m^{(1)}$ effectively down-shifts (up-shifts) the energy gaps. It dominantly affects two-exciton eigenstates that have a higher overlap with the overtone states in the site basis. We note that in the upper-left panel, compared with the reference in Fig. 2, the peaks along $\tilde{\Omega}_3 \approx (15.0, 15.3, 16.0)$ are the most affected. Specifically, their spectral weights are generally diminished, and the peaks are clustered within the range $\tilde{\Omega}_2 \approx (30.2-31.0)$. In a similar spirit, in the lower panel, we use classical transform-limited laser with parameters identical to the reference simulation in Fig. 3. The only exception is the nonlinearity parameter, which is set to larger and smaller values in the bottom-left and bottom-middle panels, respectively. We note that in the lower-left, the peaks around $(\tilde{\Omega}_2, \tilde{\Omega}_3) \approx (30.3, 15.5)$ exhibit reduced spectral weight, following a trend similar to that observed for the entangled photon pairs. The previous argument remains valid: the shift in the resonances rendered the existing laser parameters unable to track the resonance frequencies. In the lower-middle, due to the reduction of exciton nonlinearity parameter by one order of magnitude, we approach a limit where two-exciton eigenenergies are approximately equal to the sum of one-exciton energies. This implies that the respective $z_{fe'}$ resonances are of approximately equal strength to the $z_{e'g}$. As a result, the spectra are devoid of most correlation features, except for minor residuals.

The upper-right panel uses degenerate entangled photon pair frequencies to revisit the scenario presented in the top-middle panel. These frequencies are chosen such that the mediating one-exciton states become e_{13} . We note that two off-diagonal resonance zones, $(\tilde{\Omega}_2, \tilde{\Omega}_3) \approx (31.5, 15.5)$ and $(\tilde{\Omega}_2, \tilde{\Omega}_3) \approx (31.5, 16.0)$, become prominent, while the diagonal peaks at $(\tilde{\Omega}_2, \tilde{\Omega}_3) \approx (30.7, 15.5)$ are diminished. The bottom-right panel uses degenerate classical laser

frequencies to revisit the scenario from the bottom-left panel. These frequencies ensure that the mediating one-exciton states remain e_{09} . All residual off-diagonal resonances are now significantly diminished.

IV. CONCLUSION AND OUTLOOK

In this article, we demonstrated that the non-classical correlation of entangled photon pairs can be utilized to enhance the resolution of two-dimensional double quantum coherence spectra, even in the presence of dephasing. The proposed spectroscopic scheme may be realized through a combination of interferometric detection and phase-cycling techniques [15, 24, 38]. The mathematical expressions in Eq. 6 in section III A reveal that the nonlinear excitonic response involves three types of inter-manifold resonances: z_{fg} , z_{fe} , and z_{eg} . The entangled photon pairs were able to monitor and selectively amplify some of these resonances in the spectra, as shown in Fig. 2. Molecular aggregates which are composed of multiple sites, each hosting multi-level systems, the number of optical transitions are often large. When weakly coupled phonon reservoirs are present two or more dynamical resonances may involve distinct transition energies yet possess similar dephasing rates. A well characterized source of entangled photon pairs can be used to simultaneously control the photon-exciton interaction delays and combination frequencies. In turn, it may enable the discrimination between the dynamical resonances, and lead to the enhancement of the spectral resolution across either of the parametric axes, $\tilde{\Omega}_2$ or $\tilde{\Omega}_3$.

Classical transform-limited pulses, while otherwise suitable for probing ultrafast dynamics, have proved inadequate in comparable scenarios. As shown in Fig. 3 and discussed in Section III B 2, the spectral weights associated with the two pathways could not be modulated over the full parameter regime, resulting in only a partial suppression or amplification of the allowed resonances. Appropriate spectral phase modulation is known, in certain cases, to circumvent some of the previous issues by spreading the frequency components across the pulse profile. This led us to explore the role of frequency-chirped laser pulses, as also presented in section III B 2. We note that even though more sophisticated pulse-shaping protocols may prove useful [7, 37, 39–42], the signal would still exhibit a quartic scaling with the intensity of the incoming field.

The exciton response function and the resulting spectra were computed using a microscopic model of the photosynthetic complex, LHCII. The simulation accounts for both one- and two-exciton states and uses a set of realistic exciton and phonon parameters at finite temperature [16, 30]. In previous studies, ultrafast energy transfer in the one-exciton manifold was investigated spectroscopically [43–46]. They often omit the role of excited-state absorption pathways, which are essential for the generation of the DQC signal.

The simulation indicates that a complex interplay of exciton hopping, dephasing, and exciton nonlinearity governs the spectral weights of the signal. Within the Frenkel exciton model, the exciton nonlinearity parameter captures the effect of exciton correlations, the latter originating from Coulomb interactions. The two-exciton Hamiltonian is explicitly dependent on exciton nonlinearity parameters. The inter-manifold resonances, via the diagonalization step, carry this dependency into the expression of the signal. To assess the correlation origin of certain observed features, we varied the exciton nonlinearity parameter in Fig. 4 (and discussed in section III B 3) and studied the resulting spectral modulation. It is demonstrated that lowering the nonlinearity parameter caused most resonances to vanish, while increasing it gave rise to a new set of resonances. We note that due to the multi-site nature of the system, a complete suppression of the signal can not be expected. The latter bolsters the capability of the DQC signal to track spectral features arising from exciton interactions and correlations across a diverse parameter regime.

The Coulomb interactions between two participating exciton transitions, in general, may lead to several interesting multi-exciton phenomena such as exciton fusion, scattering, and annihilation. They await detailed spectroscopic investigation in the ultrafast regime. In the simulation, we strategically focused on two-exciton states, f_{39} and f_{81} , lying in the lower and upper halves of the two-exciton manifold, which may be prone to exciton-exciton annihilation (EEA). Even though the spectral signatures of EEA are typically monitored via fifth-order nonlinear optical signals, lower-order optical signals, such as DQC, can already serve as an early-stage characterization tool. The DQC technique also provides a transparent protocol for the assignment of state-specific dephasing parameters involving two-exciton states. The parameter regime explored in this work provides a transparent roadmap for measurements seeking to quantify excited-state dephasing parameters using entangled photons [47]. The latter could be useful for both spectroscopy and microscopy [48, 49].

The parameters of the entangled photon pairs are determined by the properties of JSA, depicted in Fig. 6 in Appendix C, and discussed in III A. A spectral engineering approach to the JSA would allow a consistent framework for determining the SPDC parameters [50–52].

The principal outcome of this work was the ability to explore and monitor the survival of spectral signatures originating from interfering pathways. The identification of those pathways, captured in the expression containing a sum over states, and the associated photon correlation functions offers ample room for adopting open-loop control

techniques. The control objectives may seek to optimize the photon correlation functions such that certain terms in the pathways are completely suppressed. It will provide an extension to the current approach, where the entangled photon parameters were microscopically informed yet intuitively estimated.

We note that applying the proposed technique to monitor the dynamics in correlated materials at the Mott limit provides an exciting opportunity [9, 53–55], which will be addressed in a subsequent communication.

ACKNOWLEDGMENTS

A.D. acknowledges the support from DESY (Hamburg, Germany), a member of the Helmholtz Association HGF. S.M. gratefully acknowledges the support of the National Science Foundation (NSF) grant Grant No. CHE-2246379.

Appendix A: Notes on the Hamiltonian

The exciton nonlinearity values (absolute magnitudes), $U_m^{(1)}$ and $U_{mn}^{(2)}$ used in the construction of the two-exciton Hamiltonian, i.e., $H_{mnkl}^{(2)} = H_{mn}^{(1)}\delta_{kl} + \delta_{mn}H_{kl}^{(1)} + U_m^{(1)}\delta_{mk}\delta_{nl}\delta_{mn} + U_{mn}^{(2)}\delta_{mk}\delta_{nl}$ are displayed below in Fig. 5: Only the

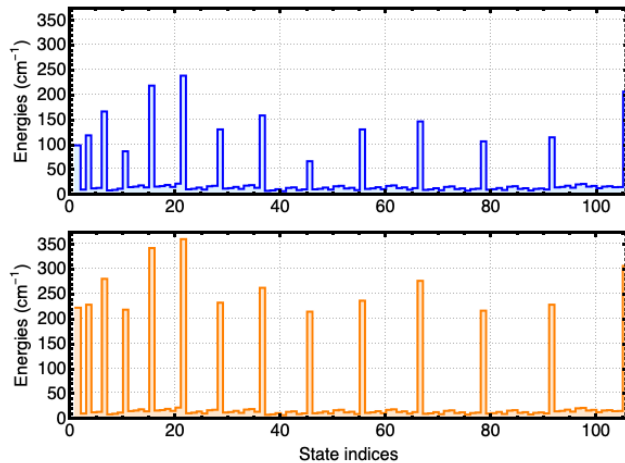


FIG. 5: The absolute exciton nonlinearity values are listed here in the order in which they appear in the local two-exciton basis. For a detailed discussion, see section II A and section III B 3.

values of $U_m^{(1)}$ differ between the two plots.

Appendix B: Outline of derivation of the signal

Here, we succinctly outline the derivation, directing the reader to [16, 25, 26] for a more involved discussion. The DQC signal is defined as the integrated rate of change of the transmitted intensity of the detected photon mode (e.g., denoted E_4), expressed as $S = \int_{-\infty}^{\infty} dt_4 \langle E_4^\dagger(t_4) E_4 \rangle$. Here, the averaging is performed over the time-dependent exciton-photon density operator. Expanding the density operator to the third power of the exciton-photon interaction, and introducing the the frequency domain variables, we obtain:

$$S = \int_{-\infty}^{\infty} dT_1 dT_2 dT_3 F(\Omega_3, \Omega_2, \Omega_1; T_3, T_2, T_1) \int_{-\infty}^{\infty} \frac{d\tilde{\omega}_3}{2\pi} \frac{d\tilde{\omega}_2}{2\pi} \frac{d\tilde{\omega}_1}{2\pi} e^{-i(-\tilde{\omega}_3 + \tilde{\omega}_2 + \tilde{\omega}_1)T_3 - i(\tilde{\omega}_1 + \tilde{\omega}_2)T_2 - i\tilde{\omega}_1 T_1} \left\{ \langle E_3^\dagger(\tilde{\omega}_3) E_4^\dagger(+\tilde{\omega}_1 + \tilde{\omega}_2 - \tilde{\omega}_3) E_2(\tilde{\omega}_2) E_1(\tilde{\omega}_1) \rangle \sum_{f, e', e, g} w^{(1)} \mathcal{G}_{e'g}(\tilde{\omega}_1 + \tilde{\omega}_2 - \tilde{\omega}_3) \mathcal{G}_{fg}(\tilde{\omega}_2 + \tilde{\omega}_1) \mathcal{G}_{eg}(\tilde{\omega}_1) \right. \\ \left. + \langle E_3^\dagger(\tilde{\omega}_3) E_4^\dagger(+\tilde{\omega}_1 + \tilde{\omega}_2 - \tilde{\omega}_3) E_2(\tilde{\omega}_2) E_1(\tilde{\omega}_1) \rangle \sum_{f, e', e, g} w^{(2)} \mathcal{G}_{fe'}(-\tilde{\omega}_3 + \tilde{\omega}_2 + \tilde{\omega}_1) \mathcal{G}_{fg}(\tilde{\omega}_2 + \tilde{\omega}_1) \mathcal{G}_{eg}(\tilde{\omega}_1) \right\}. \quad (B1)$$

In Eqn. B1, we introduced the integral transform operator,

$$F(\Omega_3, \Omega_2, \Omega_1; T_3, T_2, T_1) = \prod_{j=1}^3 \theta(T_j) \exp(i\Omega_j T_j) \quad (\text{B2})$$

where the delay variables, T_p , represent the differences between the centering times of successive photon-matter interactions. Specifically, these delays are defined as: $\tilde{\tau}_{21}^0 \rightarrow T_1, \tilde{\tau}_{32}^0 \rightarrow T_2, \tilde{\tau}_{43}^0 \rightarrow T_3$, for the diagram I, and $\tau_{21}^0 \rightarrow T_1, \tau_{42}^0 - \tau_{43}^0 \rightarrow T_2, \tau_{43}^0 \rightarrow T_3$, for the diagram II. Starting from Eq. (B1), we perform the frequency integrations to obtain the final expression for the signal, presented in Eq. 6.

Appendix C: Notes on the Joint spectral intensity function

In Fig. 6, we present the squared Joint Spectral Amplitude (JSA) for better clarity. An increase in the entanglement time parameter is inversely correlated with the number of significant singular values. As a consequence, the parametric freedom to choose the anti-correlated frequency pairs is diminished.

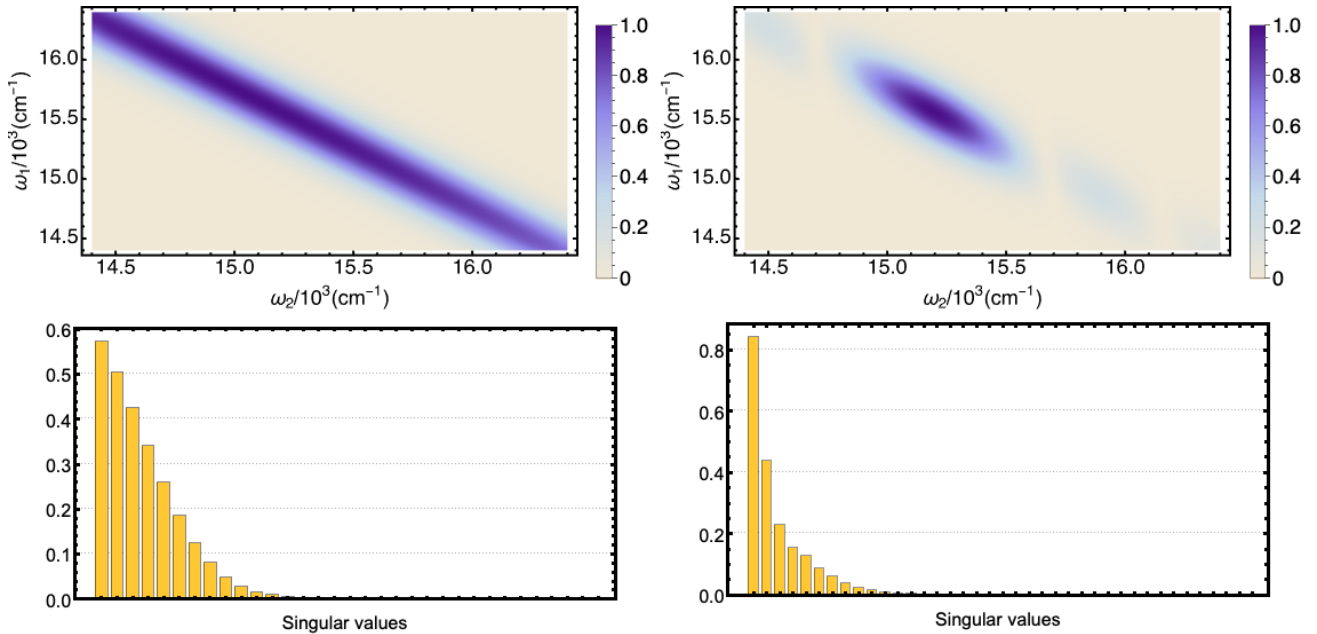


FIG. 6: The squared Joint Spectral Amplitude (JSA) is presented for two distinct entanglement time parameters: $\tilde{T}_{\text{ent}} = 10$ fs (left column) and 60 fs (right column). The lower panels display the distribution of the 20 largest normalized singular values.

[1] S. Mukamel, Communications: Signatures of quasiparticle entanglement in multidimensional nonlinear optical spectroscopy of aggregates, *The Journal of chemical physics* **132** (2010).

[2] J. Kim, S. Mukamel, and G. D. Scholes, Two-dimensional electronic double-quantum coherence spectroscopy, *Accounts of chemical research* **42**, 1375 (2009).

[3] S. Mukamel, Communication: The origin of many-particle signals in nonlinear optical spectroscopy of non-interacting particles, *The Journal of chemical physics* **145** (2016).

[4] S. Mukamel, R. Oszwaldowski, and L. Yang, A coherent nonlinear optical signal induced by electron correlations, *The Journal of chemical physics* **127** (2007).

[5] S. T. Cundiff, T. Zhang, A. D. Bristow, D. Karaiskaj, and X. Dai, Optical two-dimensional fourier transform spectroscopy of semiconductor quantum wells, *Accounts of chemical research* **42**, 1423 (2009).

[6] L. Yang and S. Mukamel, Probing many particle correlations in semiconductor quantum wells using double-quantum-coherence signal, in *Ultrafast Phenomena in Semiconductors and Nanostructure Materials XIV*, Vol. 7600 (SPIE, 2010) pp. 295–303.

- [7] D. Abramavicius, D. V. Voronine, and S. Mukamel, Double-quantum resonances and exciton-scattering in coherent 2d spectroscopy of photosynthetic complexes, *Proceedings of the National Academy of Sciences* **105**, 8525 (2008).
- [8] G. Nardin, G. Moody, R. Singh, T. M. Autry, H. Li, F. Morier-Genoud, and S. T. Cundiff, Coherent excitonic coupling in an asymmetric double ingaas quantum well arises from many-body effects, *Physical review letters* **112**, 046402 (2014).
- [9] J. Chen and P. Werner, Multidimensional coherent spectroscopy of correlated lattice systems, *npj Computational Materials* **11**, 127 (2025).
- [10] X. Dai, M. Richter, H. Li, A. D. Bristow, C. Falvo, S. Mukamel, and S. T. Cundiff, Two-dimensional double-quantum spectra reveal collective resonances in an atomic vapor, *Physical review letters* **108**, 193201 (2012).
- [11] F. Gao, S. T. Cundiff, and H. Li, Probing dipole-dipole interaction in a rubidium gas via double-quantum 2d spectroscopy, *Optics letters* **41**, 2954 (2016).
- [12] B. Lomsadze and S. T. Cundiff, Line-shape analysis of double-quantum multidimensional coherent spectra, *Physical Review A* **102**, 043514 (2020).
- [13] W. Hua, K. Bennett, Y. Zhang, Y. Luo, and S. Mukamel, Study of double core hole excitations in molecules by x-ray double-quantum-coherence signals: a multi-configuration simulation, *Chemical science* **7**, 5922 (2016).
- [14] C. Falvo, B. Palmieri, and S. Mukamel, Coherent infrared multidimensional spectra of the oh stretching band in liquid water simulated by direct nonlinear exciton propagation, *The Journal of chemical physics* **130**, 184501 (2009).
- [15] A. Debnath and A. Rubio, Entangled photon assisted multidimensional nonlinear optics of exciton-polaritons, *Journal of Applied Physics* **128** (2020).
- [16] A. Debnath and A. Rubio, Entangled biphoton enhanced double quantum coherence signal as a probe for cavity polariton correlations in presence of phonon induced dephasing, *Frontiers in Physics* **10**, 879113 (2022).
- [17] P. Saurabh and S. Mukamel, Two-dimensional infrared spectroscopy of vibrational polaritons of molecules in an optical cavity, *The Journal of chemical physics* **144**, 124115 (2016).
- [18] A. Debnath, Coherent nonlinear optical probe for cavity-dressed vibrational mode mixing: multidimensional double-quantum coherence and photon-echo signal, *arXiv preprint arXiv:2504.17907* (2025).
- [19] E. R. Bittner, H. Li, A. Piryatinski, A. R. Srimath Kandada, and C. Silva, Probing exciton/exciton interactions with entangled photons: Theory, *The Journal of Chemical Physics* **152**, 071101 (2020).
- [20] A. Ishizaki, Probing excited-state dynamics with quantum entangled photons: Correspondence to coherent multidimensional spectroscopy, *The Journal of Chemical Physics* **153** (2020).
- [21] Y. Fujihashi and A. Ishizaki, Achieving two-dimensional optical spectroscopy with temporal and spectral resolution using quantum entangled three photons, *The Journal of Chemical Physics* **155** (2021).
- [22] Y. Fujihashi, K. Miwa, M. Higashi, and A. Ishizaki, Probing exciton dynamics with spectral selectivity through the use of quantum entangled photons, *The Journal of Chemical Physics* **159** (2023).
- [23] Y. Fujihashi, A. Ishizaki, and R. Shimizu, Pathway selectivity in time-resolved spectroscopy using two-photon coincidence counting with quantum entangled photons, *The Journal of Chemical Physics* **160** (2024).
- [24] K. E. Dorfman and S. Mukamel, Multidimensional spectroscopy with entangled light: loop vs ladder delay scanning protocols, *New journal of physics* **16**, 033013 (2014).
- [25] K. E. Dorfman, F. Schlawin, and S. Mukamel, Nonlinear optical signals and spectroscopy with quantum light, *Reviews of Modern Physics* **88**, 045008 (2016).
- [26] M. Richter and S. Mukamel, Ultrafast double-quantum-coherence spectroscopy of excitons with entangled photons, *Physical Review A* **82**, 013820 (2010).
- [27] A. Debnath and S. Mukamel, Entangled photon pair excitation and time-frequency filtered multidimensional photon correlation spectroscopy as a probe for dissipative exciton kinetics, *arXiv preprint arXiv:2601.20700* (2026).
- [28] T. Landes, M. G. Raymer, M. Allgaier, S. Merkouche, B. J. Smith, and A. H. Marcus, Quantifying the enhancement of two-photon absorption due to spectral-temporal entanglement, *Optics Express* **29**, 20022 (2021).
- [29] M. G. Raymer and T. Landes, Theory of two-photon absorption with broadband squeezed vacuum, *Physical Review A* **106**, 013717 (2022).
- [30] V. Novoderezhkin, A. Marin, and R. van Grondelle, Intra-and inter-monomeric transfers in the light harvesting lhcii complex: the redfield-förster picture, *Physical Chemistry Chemical Physics* **13**, 17093 (2011).
- [31] V. I. Novoderezhkin, M. A. Palacios, H. Van Amerongen, and R. Van Grondelle, Excitation dynamics in the lhcii complex of higher plants: modeling based on the 2.72 Å crystal structure, *The Journal of Physical Chemistry B* **109**, 10493 (2005).
- [32] A. Pe'er, B. Dayan, A. A. Friesem, and Y. Silberberg, Temporal shaping of entangled photons, *Physical review letters* **94**, 073601 (2005).
- [33] B. Dayan, A. Pe'er, A. A. Friesem, and Y. Silberberg, Nonlinear interactions with an ultrahigh flux of broadband entangled photons, *Physical review letters* **94**, 043602 (2005).
- [34] A. Christ, K. Laiho, A. Eckstein, K. N. Cassemiro, and C. Silberhorn, Probing multimode squeezing with correlation functions, *New Journal of Physics* **13**, 033027 (2011).
- [35] B. Chatel, J. Degert, S. Stock, and B. Girard, Competition between sequential and direct paths in a two-photon transition, *Physical Review A* **68**, 041402 (2003).
- [36] A. Debnath, *Dynamics and control of open quantum systems: applications to exciton dynamics in quantum dots and vibrational dynamics in carboxyhemoglobin*, Ph.D. thesis, Toulouse 3 (2013).
- [37] A. Debnath, C. Meier, B. Chatel, and T. Amand, High-fidelity biexciton generation in quantum dots by chirped laser pulses, *Physical Review B* **88**, 201305 (2013).
- [38] M. G. Raymer, A. H. Marcus, J. R. Widom, and D. L. Vitullo, Entangled photon-pair two-dimensional fluorescence spectroscopy (epp-2dfs), *The Journal of Physical Chemistry B* **117**, 15559 (2013).

- [39] A. Debnath, C. Meier, B. Chatel, and T. Amand, Chirped laser excitation of quantum dot excitons coupled to a phonon bath, *Physical Review B* **86**, 161304 (2012).
- [40] A. Hedse, A. A. S. Kalaei, A. Wacker, and T. Pullerits, Pulse overlap artifacts and double quantum coherence spectroscopy, *The Journal of chemical physics* **158** (2023).
- [41] J. Lavoie, T. Landes, A. Tamimi, B. J. Smith, A. H. Marcus, and M. G. Raymer, Phase-modulated interferometry, spectroscopy, and refractometry using entangled photon pairs, *Advanced Quantum Technologies* **3**, 1900114 (2020).
- [42] D. Fersch, P. Maly, J. Ruhe, V. Lisinetskii, M. Hensen, F. Wurthner, and T. Brixner, Single-molecule ultrafast fluorescence-detected pump-probe microscopy, *The Journal of Physical Chemistry Letters* **14**, 4923 (2023).
- [43] T. N. Do, A. Huerta-Viga, P. Akhtar, H. L. Nguyen, P. J. Nowakowski, M. F. Khyasudeen, P. H. Lambrev, and H.-S. Tan, Revealing the excitation energy transfer network of light-harvesting complex ii by a phenomenological analysis of two-dimensional electronic spectra at 77 k, *The Journal of Chemical Physics* **151** (2019).
- [44] P. Malý, J. M. Gruber, R. van Grondelle, and T. Mančal, Single molecule spectroscopy of monomeric lhcii: Experiment and theory, *Scientific Reports* **6**, 26230 (2016).
- [45] Z. Zhang, P. H. Lambrev, K. L. Wells, G. Garab, and H.-S. Tan, Direct observation of multistep energy transfer in lhcii with fifth-order 3d electronic spectroscopy, *Nature communications* **6**, 7914 (2015).
- [46] E. A. Arsenault, Y. Yoneda, M. Iwai, K. K. Niyogi, and G. R. Fleming, The role of mixed vibronic qy-qx states in green light absorption of light-harvesting complex ii, *Nature communications* **11**, 6011 (2020).
- [47] X. Liu, T. Li, J. Wang, M. R. Kamble, A. M. Zheltikov, and G. S. Agarwal, Probing ultra-fast dephasing via entangled photon pairs, *Optics Express* **30**, 47463 (2022).
- [48] C. Tsao, H. Ling, A. Hinkle, Y. Chen, K. K. Jha, Z.-L. Yan, and H. Utzat, Enhancing spectroscopy and microscopy with emerging methods in photon correlation and quantum illumination, *Nature Nanotechnology* , 1 (2025).
- [49] C. A. Casacio, L. S. Madsen, A. Terrasson, M. Waleed, K. Barnscheidt, B. Hage, M. A. Taylor, and W. P. Bowen, Quantum-enhanced nonlinear microscopy, *Nature* **594**, 201 (2021).
- [50] A. Dosseva, L. Cincio, and A. M. Branczyk, Shaping the joint spectrum of down-converted photons through optimized custom poling, *arXiv preprint arXiv:1410.7714* (2014).
- [51] A. Shukhin, I. Hurvitz, S. Trajtenberg-Mills, A. Arie, and H. Eisenberg, Two-dimensional control of a biphoton joint spectrum, *Optics Express* **32**, 10158 (2024).
- [52] T. F. Weiss and A. Peruzzo, Nonlinear domain engineering for quantum technologies, *Applied Physics Reviews* **12** (2025).
- [53] G. Citeroni, M. Polini, M. Dapolito, D. Basov, and G. Mazza, Ultrafast dynamics of quantum matter driven by time-energy entangled photons, *arXiv preprint arXiv:2506.12211* (2025).
- [54] A. Debnath and R. Santra, Theory of high-energy correlated multiphoton x-ray diffraction for synchrotron-radiation sources, *Physical review research* **5**, 023158 (2023).
- [55] G. Nambiar, A. Grankin, and M. Hafezi, Diagnosing electronic phases of matter using photonic correlation functions, *Physical Review X* **15**, 041020 (2025).